


RESEARCH ARTICLE

Numerical study of hydrodynamic flow of a Casson nanomaterial past an inclined sheet under porous medium

Muhammad Imran Anwar^{1,2,3} | Khuram Rafique³ |
Masnita Misiran³ | Sabir Ali Shehzad⁴ 

¹Department of Mathematics, Faculty of Science, University of Sargodha, Sargodha, Pakistan

²Higher Education Department (HED) Punjab, Lahore, Pakistan

³School of Quantitative Sciences, Universiti Utara Malaysia, Sintok, Kedah, Malaysia

⁴Department of Mathematics, COMSATS University Islamabad, Sahiwal, Pakistan

Correspondence

Sabir Ali Shehzad, Department of Mathematics, COMSATS University Islamabad, Sahiwal 57000, Pakistan.
Email: sabirali@cuisahiwal.edu.pk

Abstract

The main aim of the current paper is to investigate the mass and heat transportation of a Casson nanomaterial generated by the inclination of the surface. The magnetic field effect along with suction or injection are considered. The working nanomaterial is taken into consideration based on the concept of the Buongiorno nanofluid theory, which explores the thermal efficiencies of liquid flows under movement of Brownian and thermophoretic phenomena. The emergent system of differential expressions is converted to dimensionless form with the help of the appropriate transformations. This system is numerically executed by the implementation of Keller–Box and Newton's schemes. A good agreement of results can be found with the previous data in a limiting approach. The behavior of the physical quantities under concern, including energy exchange, Sherwood number, and wall shear stress are portrayed through graphs and in tabular form. The Nusselt number and Sherwood number are found to diminish against the altered magnitudes of Brownian motion and the inclination parameter. Moreover, the velocity profile decreases with the growth of the inclination effect. In the same vein, the buoyancy force and solutal buoyancy effects show a direct relation with the velocity field. The

outcomes have promising technological uses in liquid-based systems related to stretchable constituents.

KEYWORDS

Casson nanofluid, inclined surface, Keller–Box method, MHD

1 | INTRODUCTION

The boundary-driven flow analysis over moving surfaces with combined effects of heat mass transport has generated noticeable attention from many scholars due to its extensive variety of uses in engineering and manufacturing, such as broadsheet production, hot rolling, exclusion of malleable pieces, and metal sheets in bath. Sakiadis¹ initiated the efforts to exploit the boundary-driven fluid flow over a constantly stirring surface. Moreover, Crane² studied this phenomenon for viscous fluid over a stretchable sheet. Mucoglu and Chen³ analyzed the bouncy force in laminar forced convected flow toward an inclined surface and found that for assisting flow, the skin friction and Nusselt number enhance with the growth of buoyancy effect. The inner heat generation phenomenon in natural convected flow under magnetized impact was executed by Chamkha and Khaled.⁴ They found that the wall shear stress reduces with the wall suction effect. Alam et al⁵ described the numerical behavior of magnetized convective flow generated by the inclination of the sheet. They concluded that the heat generation boosted the velocity field. Ramesh et al⁶ investigated the momentum and heat exchange of dusty liquid flow with the inclination of a moving surface and found an interesting outcome—the dusty fluid velocity is enhanced, whereas, the velocity of clean diminishes with the growth of the fluid interaction factor. Ali et al⁷ investigated the conjugate aspects of heat-mass transport in magnetized convected flow over an inclined surface. They used an analytical approach for the solution. For further detailed literature on the inclination effect with different geometries, please see Refs.^{8–12}

Nowadays, nanofluids have attained great importance from recent researchers due to their advanced thermal presentation and having impressive potential to the amount of heat transfer deprived of pressure falls. A nanofluid is a combination of different nanoparticles, including Al_2O_3 , Cu, and CuO, in a base fluid such as, oil, water, ethylene, glycol etc. It is verified by research that the thermal conductivity of the base liquid is considerably less than the nanofluid of Choi and Eastman.¹³ The nanofluid is utilized as the working fluid instead of the base fluid because of its higher thermal conductivity. In fact, a working liquid is used in various engineering and industrial procedures. The heat/energy can be transferred from one place to another by using this fluid. The nanofluid is the best option for this. Nanofluids are employed in nanotechnology, hyperthermia cancer cure, microelectronics, medical procedures, and hybrid power devices. Buongiorno¹⁴ studied the mechanism of nanofluids through Brownian and thermophoresis factors. Murthy et al¹⁵ probed the free convection flow of nanofluids toward a slanted sheet. They found that the heat and mass exchange rate reduces on prompting the inclination effect. Rashad¹⁶ studied the unsteady flow of nanofluid toward a slanted sheet. He found that the skin friction improved with enhancement in the Biot number. Usman et al¹⁷ studied the flow of a Casson nanofluid toward an inclined stretching cylinder. They considered the Brownian motion and thermophoretic effects. Khan et al¹⁸ examined the flow of Jeffery nanofluid toward an inclined stretching surface. They considered the Cattaneo–Christov model

and solved it numerically by using the shooting technique. Ghadikolaei et al¹⁹ investigated the flow of a Casson nanofluid toward a slanted sheet. For detailed knowledge, see Refs.²⁰⁻³⁰

In 1959, Casson executed the Casson fluid model. This model expresses the nature of shear thinning materials, which are assumed to have zero viscosity at an infinite amount of shear and immeasurable viscosity at a zero shear rate and yield stress through which no flow takes place. Shear thinning conveys the reaction of a fluid substance viscosity (also known as resistance to flow) when force is applied. A few materials like jam, tomato paste, broth, rigorous fruit liquids, and human blood, etc. represent Casson fluid.³¹ These fluids with energy exchange are extensively used in syrups, nails, processing of chocolate, foams, and several other food stuff.³² Reddy³³ investigated the flow of a Casson fluid toward an exponential slanted sheet. He found that the Casson factor enhances the skin friction factor. Saeed et al³⁴ studied the three-dimensional flow of a Casson nanofluid toward a slanted disk. They found that energy transportation shows a direct relation with the radiation effect. Rawi et al³⁵ discussed the flow of a Casson liquid toward a slanted sheet and observed that the Casson impact creates reduction in the velocity field. Shehzad et al³⁶ explored the Casson fluid above a porous sheet and found a sequence of results. For the latest studies on the flow of Casson fluid with different geometries, see Refs.³⁷⁻³⁹

Having all such practical values of Casson fluid flow under nanoparticles, our aim was to study the flow of a magnetized Casson nanomaterial induced by the inclination of a moving sheet. The numerical results that govern the physical model are elaborated through the Keller–Box scheme. To the best of the author’s knowledge, there is no study in the literature on the heat and mass exchange of magnetized Casson nanomaterial flow over an inclined surface with the Keller–Box scheme. The Casson nanofluid is more helpful for cooling and friction reducing agents as compared to Newtonian based nanofluid flow.⁴⁰ The current problem model is developed from the Khan and Pop model.⁴¹ The Keller–Box scheme has been extensively used and it is more flexible and friendly to use as compared to other numerical techniques. It is much quicker, more efficient, easier to program, and easier to practice.

2 | MODELING

A steady-state flow of a Casson nanomaterial generated by the inclination of sheet having an angle “ α ” with the vertical direction is assumed. The stretched and free-stream velocities are supposed to be of the forms $u_w(x) = ax$ and $u_\infty(x) = 0$, respectively, in which “ α ” is the constant and x , the co-ordinate along the sheet (see Figure 1). The Brownian motion and thermophoresis are also accounted for. The wall temperature is T_w , C_w denotes nanoparticle concentration, and u_w denotes the velocity on the wall, respectively. Moreover, the free stream temperature is denoted by T_∞ and C_∞ exhibits the nanoparticle concentration as y keeps an eye on infinity.

The flow equations for this study are given by^{31,35,41}:

$$\frac{\partial u}{\partial x} + \frac{\partial v}{\partial y} = 0, \quad (1)$$

$$u \frac{\partial u}{\partial x} + v \frac{\partial v}{\partial y} = \left(1 + \frac{1}{\beta}\right) \nu \frac{\partial^2 u}{\partial y^2} + g [\beta_t (T - T_\infty) + \beta_c (C - C_\infty)] \cos \alpha - \left(\frac{\sigma B_0^2(x)}{\rho} + \frac{\mu}{\rho k}\right) u, \quad (2)$$

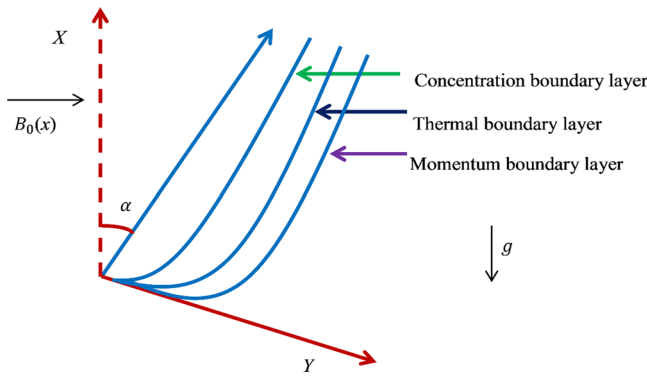


FIGURE 1 Physical geometry with co-ordinate system [Color figure can be viewed at wileyonlinelibrary.com]

$$u \frac{\partial T}{\partial x} + v \frac{\partial T}{\partial y} = \alpha^* \frac{\partial^2 T}{\partial y^2} + \tau \left[D_B \frac{\partial C}{\partial y} \frac{\partial T}{\partial y} + \frac{D_T}{T_\infty} \left(\frac{\partial T}{\partial y} \right)^2 \right], \quad (3)$$

$$u \frac{\partial C}{\partial x} + v \frac{\partial C}{\partial y} = D_B \frac{\partial^2 C}{\partial y^2} + \frac{D_T}{T_\infty} \frac{\partial^2 T}{\partial y^2}, \quad (4)$$

where, in the directions x and y , the velocity constituents are u and v individually, g is the gravitational acceleration, the strength of magnetic field is defined by B_0 , σ is the electrical conductivity, viscosity is given by μ , the density of conventional fluid is given by ρ_f , density of the nanoparticle is given by ρ_p , the thermal expansion factor is denoted by β_t , the concentration expansion constant is given by β_c , D_B denotes the Brownian dissemination factor, and D_T represents the thermophoresis dispersion factor, k denotes the thermal conductivity, the symbolical representation of heat capacity of the nanoparticles is $(\rho c)_p$, $(\rho c)_f$ denotes the heat capacity of the conventional liquid, $\alpha^* = k/(\rho c)_f$ denotes the thermal diffusivity parameter, the symbolic representation of the relation among current heat capacity of the nanoparticle and the liquid is $\tau = (\rho c)_p/(\rho c)_f$.

The boundary settings are

$$\begin{aligned} u = u_w(x) = ax, \quad v = v_w, \quad T = T_w, \quad C = C_w \quad \text{at } y = 0, \\ u \rightarrow u_\infty(x) = 0, \quad v \rightarrow 0, \quad T \rightarrow T_\infty, \quad C \rightarrow C_\infty \quad \text{as } y \rightarrow \infty. \end{aligned} \quad (5)$$

The stream function $\psi = \psi(x, y)$ is defined as:

$$u = \frac{\partial \psi}{\partial y}, \quad v = -\frac{\partial \psi}{\partial x}, \quad (6)$$

where, Equation (1) is fulfilled. The similarity transformations are defined as:

$$u = axf'(\eta), \quad v = -\sqrt{av}f(\eta), \quad \eta = y\sqrt{\frac{a}{\nu}}$$

$$\theta(\eta) = \frac{T - T_\infty}{T_w - T_\infty}, \quad \varphi(\eta) = \frac{C - C_w}{C_w - C_\infty}. \quad (7)$$

Substituting Equation (7), Equation (1) is satisfied identically and expressions (2) to (4) reduce to the following system:

$$\left(1 + \frac{1}{\beta}\right)f''' + ff'' - f'^2 + (\lambda\theta + \delta\varphi)\cos\alpha - (M + K)f' = 0, \quad (8)$$

$$\left(\frac{1}{\text{Pr}}\right)\theta'' + f\theta' + Nb\varphi'\theta' + Nt\theta'^2 = 0, \quad (9)$$

$$\varphi'' + Le f\varphi' + Nt_b\theta'' = 0. \quad (10)$$

Here,

$$\begin{aligned} \lambda &= \frac{Gr_x}{Re_x^2}, \quad \delta = \frac{Gc_x}{Re_x^2}, \quad M = \frac{\sigma B_0^2(x)}{a\rho}, \quad K = \frac{\nu}{ak}, \quad Le = \frac{\nu}{D_B}, \quad \text{Pr} = \frac{\nu}{\alpha^*}, \\ Nb &= \frac{\tau D_B (C_w - C_\infty)}{\nu}, \\ Nt &= \frac{\tau D_T (T_w - T_\infty)}{\nu T_\infty}, \quad Gr_x = \frac{g\beta_t (T_w - T_\infty)x^3}{\nu^2}, \quad Re_x = \frac{u_w(x)x}{\nu}, \\ Gc_x &= \frac{g\beta_c (C_w - C_\infty)x^3}{\nu^2}, \quad Nt_b = \frac{Nt}{Nb}. \end{aligned} \quad (11)$$

Here, primes denote the differentiation with respect to η , M denotes the magnetic factor, ν denotes the liquid kinematic viscosity, Prandtl number is denoted by Pr, the Lewis number is denoted by Le , and the permeability parameter is represented by K .

The corresponding boundary settings are changed to

$$\begin{aligned} f(\eta) &= S, \quad f'(\eta) = 1, \quad \theta(\eta) = 1, \quad \varphi(\eta) = 1, \quad \text{at } \eta = 0, \\ f'(\eta) &\rightarrow 0, \quad \theta(\eta) \rightarrow 0, \quad \varphi(\eta) \rightarrow 0, \quad \text{at } \eta \rightarrow \infty. \end{aligned} \quad (12)$$

The physical quantities of concern are skin friction C_f , Nusselt number Nu , and Sherwood number Sh demarcated as:

$$C_f = \frac{\tau_w}{\rho u_w^2}, \quad Nu = \frac{xq_w}{k(T_w - T_\infty)}, \quad Sh = \frac{xq_m}{D_B(C_w - C_\infty)}, \quad (13)$$

where $\tau_w = \mu(1 + \frac{1}{\beta})\frac{\partial T}{\partial y}$, $q_w = -\alpha^*\frac{\partial T}{\partial y}$, $q_m = -D_B\frac{\partial C}{\partial y}$ at $y = 0$ are the shear stress, heat, and mass fluxes at the surface, respectively. The associated expressions of the skin-friction coefficient C_f , the reduced Nusselt number $-\theta'(0)$, and the reduced Sherwood number $-\varphi'(0)$ are defined as

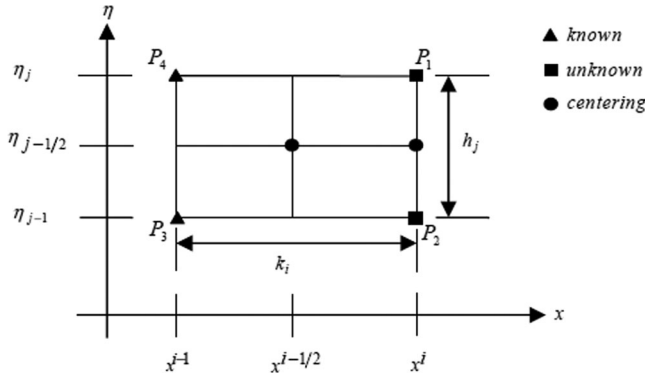


FIGURE 2 Net rectangle of difference approximations

$$-\theta'(0) = \frac{Nu_x}{\sqrt{Re_x}}, \quad -\varphi'(0) = \frac{Sh_x}{\sqrt{Re_x}}, \quad C_f\sqrt{Re_x} = \left(1 + \frac{1}{\beta}\right)f''(0), \quad (14)$$

where $Re_x = u_w(x)x/\nu$ is the local Reynolds number based on the stretching velocity.

3 | NUMERICAL PROCEDURES

The numerical structure of the Keller–Box technique for the formulated problem of Casson liquid is explained for the finite-difference technique, block-elimination scheme, and Newton’s method.⁴²

3.1 | The finite difference method

Expressions (8) to (10) are modified into a system of the first-order differential equations by the implementation of conditions (12). Here, we use novel dependent variables such as $f(\eta)$, $u(\eta)$, $v(\eta)$, $g(\eta)$, $p(\eta)$, $q(\eta)$, and $s(\eta)$. Also, $\varphi(\eta)$ and $\theta(\eta)$ are substituted with $q(\eta)$ and $g(\eta)$, respectively, that represent the fluid concentration and temperature, respectively. Therefore, in the following, the first-order expressions are:

$$f'(\eta) = u(\eta), \quad u'(\eta) = v(\eta), \quad g'(\eta) = p(\eta), \quad q'(\eta) = s(\eta), \quad (15)$$

$$\left(1 + \frac{1}{\beta}\right)v' + fv - u^2 + (\lambda g + \delta q)\cos \alpha - (M + K)u = 0, \quad (16)$$

$$\left(\frac{1}{Pr}\right)p' + fp + Nbsp + Ntp^2 = 0, \quad (17)$$

$$s' + Lefs + Nt_b p' = 0. \quad (18)$$

Equation (12) in expressions of variable η becomes

$$\begin{aligned} f(\eta) = s, \quad u(\eta) = 1, \quad g(\eta) = 1, \quad q(\eta) = 1, \quad \text{at } \eta = 0, \\ u(\eta) \rightarrow 0, \quad g(\eta) \rightarrow 0, \quad q(\eta) \rightarrow 0, \quad \text{as } \eta \rightarrow \infty. \end{aligned} \quad (19)$$

Figure 2 is taken in the x - η plane and the mesh points are considered as under:

$$x^0 = 0, \quad x^i = x^{i-1} + k_i, \quad i = 1, 2, 3, \dots, I, \quad (20)$$

$$\eta_0 = 0, \quad \eta_j = \eta_{j-1} + h_j, \quad j = 1, 2, 3, \dots, J, \quad \eta_J \equiv \eta_\infty, \quad (21)$$

where $\Delta\eta$ -spacing is h_j and k_i is the Δx -spacing. Here i and j are just used to show the coordinate position.

By the finite difference approach, the derivatives in x -direction are set as:

$$\frac{\partial u}{\partial x} = \frac{u^i - u^{i-1}}{k_i}. \quad (22)$$

The η -direction derivatives are substituted by using finite difference as:

$$v' = \frac{\partial v}{\partial \eta} = \frac{v_j - v_{j-1}}{h_j}, \quad (23)$$

for any points:

$$()_{j-1/2}^{i-1/2} = \frac{1}{2} [()_{j-1}^i + ()_j^{i-1}], \quad (24)$$

and

$$()_{j-1/2}^i = \frac{1}{2} [()_{j-1}^i + ()_j^i], \quad (25)$$

The difference Equations (15) to (18) are called approximate equations and are inscribed by taking one net rectangle as shown in Figure 2. The finite difference approximations of differential expressions (15) to (18) by using centered-difference derivatives are written for the center ($\eta_{j-1/2}$) of the section P_1P_2 . This procedure is named “centering about ($\eta_{j-1/2}$)” defined as

$$\begin{aligned}
 \frac{(f_j^i - f_{j-1}^i)}{h_j} &= \frac{1}{2}(u_j^i - u_{j-1}^i) = u_{j-\frac{1}{2}}^i, \\
 \frac{(u_j^i - u_{j-1}^i)}{h_j} &= \frac{1}{2}(v_j^i - v_{j-1}^i) = v_{j-\frac{1}{2}}^i, \\
 \frac{(g_j^i - g_{j-1}^i)}{h_j} &= \frac{1}{2}(p_j^i - p_{j-1}^i) = p_{j-\frac{1}{2}}^i, \\
 \frac{(q_j^i - q_{j-1}^i)}{h_j} &= \frac{1}{2}(s_j^i - s_{j-1}^i) = s_{j-\frac{1}{2}}^i, \\
 \left(1 + \frac{1}{\beta}\right) \frac{(v_j^i - v_{j-1}^i)}{h_j} &+ \left[\left(\frac{(f_j^i + f_{j-1}^i)}{2} \right) \left(\frac{(v_j^i + v_{j-1}^i)}{2} \right) \right] - \left(\frac{(u_j^i + u_{j-1}^i)}{2} \right)^2 \\
 &+ \left[\lambda \left(\frac{(g_j^i + g_{j-1}^i)}{2} \right) + \delta \left(\frac{(q_j^i + q_{j-1}^i)}{2} \right) \right] \cos \alpha - \gamma \left(\frac{(u_j^i + u_{j-1}^i)}{2} \right)^2 = 0, \\
 \left(\frac{1}{Pr}\right) \frac{(p_j^i - p_{j-1}^i)}{h_j} &+ \left[\left(\frac{(f_j^i + f_{j-1}^i)}{2} \right) \left(\frac{(p_j^i + p_{j-1}^i)}{2} \right) \right] + Nb \left[\left(\frac{(s_j^i + s_{j-1}^i)}{2} \right) \left(\frac{(p_j^i + p_{j-1}^i)}{2} \right) \right] \\
 &+ Nt \left[\left(\frac{(p_j^i + p_{j-1}^i)}{2} \right)^2 \right] = 0, \\
 \frac{(s_j^i - s_{j-1}^i)}{h_j} &+ Le \left[\left(\frac{(f_j^i + f_{j-1}^i)}{2} \right) \left(\frac{(s_j^i + s_{j-1}^i)}{2} \right) \right] + Nt \left[\frac{(p_j^i - p_{j-1}^i)}{h_j} \right] = 0.
 \end{aligned}
 \tag{26}$$

In terms of the dependent variable (η), the subjected boundary conditions (19) at $x=x^i$, become

$$\begin{aligned}
 f_0^i &= 0, & u_0^i &= 1, & g_0^i &= 1, & q_0^i &= 1, \\
 u_j^i &= 0, & g_j^i &= 0, & q_j^i &= 0.
 \end{aligned}
 \tag{27}$$

3.2 | Newton’s method

If $f_j^{i-1}, u_j^{i-1}, v_j^{i-1}, g_j^{i-1}, p_j^{i-1}, q_j^{i-1}, s_j^{i-1}$ are supposed to be known for $0 \leq j \leq J$, then the result of the unknown $(f_j^i, u_j^i, v_j^i, g_j^i, p_j^i, q_j^i, s_j^i)$, $0 \leq j \leq J$, have to be achieved. For simplicity

TABLE 1 Comparison of $-\theta'(0)$ and $-\phi'(0)$ when $M = S = K = \delta = \lambda = 0$, $Le = Pr = 10$ and $\alpha = 90^\circ$ as $\beta \rightarrow \infty$

<i>Nb</i>	<i>Nt</i>	Khan and Pop ⁴¹		Present results	
		$-\theta'(0)$	$-\phi'(0)$	$-\theta'(0)$	$-\phi'(0)$
0.1	0.1	0.9524	2.1294	0.9524	2.1294
0.2	0.2	0.3654	2.5152	0.3654	2.5152
0.3	0.3	0.1355	2.6088	0.1355	2.6088
0.4	0.4	0.0495	2.6038	0.0495	2.6038
0.5	0.5	0.0179	2.5731	0.0179	2.5731

of representations, and reducing the quadratic and higher order terms in $\delta'f_j^k$, $\delta'u_j^k$, $\delta'v_j^k$, $\delta'g_j^k$, $\delta'p_j^k$, $\delta'q_j^k$, and $\delta's_j^k$ as well as the superscript i gives:

$$\begin{aligned}
 \delta'f_j - \delta'f_{j-1} - \frac{h_j}{2}(\delta'u_j - \delta'u_{j-1}) &= (r_1)_{j-\frac{1}{2}}, \\
 \delta'u_j - \delta'u_{j-1} - \frac{h_j}{2}(\delta'v_j - \delta'v_{j-1}) &= (r_2)_{j-\frac{1}{2}}, \\
 \delta'g_j - \delta'g_{j-1} - \frac{h_j}{2}(\delta'p_j - \delta'p_{j-1}) &= (r_3)_{j-\frac{1}{2}}, \\
 \delta'q_j - \delta'q_{j-1} - \frac{h_j}{2}(\delta's_j - \delta's_{j-1}) &= (r_4)_{j-\frac{1}{2}}, \tag{28} \\
 (a_1)_j\delta'v_j + (a_2)_j\delta'v_{j-1} + (a_3)_j\delta'f_j + (a_4)_j\delta'f_{j-1} + (a_5)_j\delta'u_j + (a_6)_j\delta'u_{j-1} + (a_7)_j\delta'g_j \\
 + (a_8)_j\delta'g_{j-1} + (a_9)_j\delta'q_j + (a_{10})_j\delta'q_{j-1} &= (r_5)_{j-\frac{1}{2}}, \\
 (b_1)_j\delta'p_j + (b_2)_j\delta'p_{j-1} + (b_3)_j\delta'f_j + (b_4)_j\delta'f_{j-1} + (b_5)_j\delta's_j + (b_6)_j\delta's_{j-1} &= (r_6)_{j-\frac{1}{2}}, \\
 (c_1)_j\delta's_j + (c_2)_j\delta's_{j-1} + (c_3)_j\delta'f_j + (c_4)_j\delta'f_{j-1} + (c_5)_j\delta'p_j + (c_6)_j\delta'p_{j-1} &= (r_7)_{j-\frac{1}{2}},
 \end{aligned}$$

where

$$(a_1)_j = 1 + \frac{h_j}{2\beta^*}f_{j-\frac{1}{2}}, \quad (a_2)_j = 1 + \frac{h_j}{2\beta^*}f_{j-\frac{1}{2}} - 2, \quad (a_3)_j = \frac{h_j}{2\beta^*}v_{j-\frac{1}{2}}, \quad (a_4)_j = (a_3)_j,$$

$$(a_5)_j = \frac{-h_j}{\beta^*}u_{j-\frac{1}{2}} - \frac{\gamma}{2\beta^*}h_j, \quad (a_6)_j = (a_5)_j, \quad (a_7)_j = \left(\frac{\lambda}{2\beta^*}\right)h_j \cos \alpha, \quad (a_8)_j = (a_7)_j,$$

$$(a_9)_j = \left(\frac{\delta}{2\beta^*}\right)h_j \cos \alpha, \quad (a_{10})_j = (a_9)_j,$$

TABLE 2 Values of $-\theta'(0)$, $-\phi'(0)$, and $C_{fx}(0)$ for multiple values of involved constraints

Nb	Nt	Pr	Le	M	K	β	λ	δ	S	α	$-\theta'(0)$	$-\phi'(0)$	$C_{fx}(0)$
0.1	0.1	6.5	5.0	0.5	1.0	5.0	1.0	1.0	0.5	45°	2.6559	1.3140	1.3697
0.5	0.1	6.5	5.0	0.5	1.0	5.0	1.0	1.0	0.5	45°	0.5634	3.4011	1.3755
0.1	0.5	6.5	5.0	0.5	1.0	5.0	1.0	1.0	0.5	45°	1.3936	-1.2192	1.1353
0.1	0.1	6.5	5.0	0.5	1.0	10.0	1.0	1.0	0.5	45°	2.6531	1.3001	1.4300
0.1	0.1	6.5	5.0	0.5	1.0	5.0	4.0	1.0	0.5	45°	2.6694	1.3521	1.0218
0.1	0.1	6.5	5.0	0.5	1.0	5.0	1.0	5.0	0.5	45°	2.6851	1.4121	0.6953
0.1	0.1	6.5	5.0	0.5	1.0	5.0	1.0	1.0	1.5	45°	6.4881	1.8501	2.0180
0.1	0.1	6.5	5.0	0.5	1.0	5.0	1.0	1.0	0.0	45°	1.0784	1.0507	1.0471
0.1	0.1	6.5	5.0	0.5	1.0	5.0	1.0	1.0	-1.5	45°	0.0252	0.0017	0.4203
0.1	0.1	6.5	5.0	0.5	1.0	5.0	1.0	1.0	0.5	60°	2.6521	1.3014	1.4556
0.1	0.1	6.5	5.0	0.5	1.0	5.0	1.0	1.0	0.5	90°	2.6447	1.2693	1.6665

$$\begin{aligned}
(b_1)_j &= 1 + \text{Pr} \frac{h_j}{2} f_{j-\frac{1}{2}} + \frac{Nb \text{Pr} h_j}{2} s_{j-\frac{1}{2}} + h_j Nt \text{Pr} p_{j-\frac{1}{2}}, & (b_2)_j &= (b_1)_j - 2, \\
(b_3)_j &= \text{Pr} \frac{h_j}{2} p_{j-\frac{1}{2}}, & (b_4)_j &= (b_3)_j, & (b_5)_j &= \frac{Nb \text{Pr} h_j}{2} p_{j-\frac{1}{2}}, & (b_6)_j &= (b_5)_j, \\
(c_1)_j &= 1 + \frac{h_j Le}{2} f_{j-\frac{1}{2}}, & (c_2)_j &= (c_1)_j - 2, & (c_3)_j &= \frac{h_j Le}{2} s_{j-\frac{1}{2}}, & (c_4)_j &= (c_3)_j, \\
(c_5)_j &= Nt_b, & (c_6)_j &= -Nt_b, \\
(R_1)_{j-\frac{1}{2}} &= f_{j-1} - f_j + h_j u_{j-\frac{1}{2}}, \\
(R_2)_{j-\frac{1}{2}} &= u_{j-1} - u_j + h_j v_{j-\frac{1}{2}}, \\
(R_3)_{j-\frac{1}{2}} &= g_{j-1} - g_j + h_j p_{j-\frac{1}{2}}, \\
(R_4)_{j-\frac{1}{2}} &= q_{j-1} - q_j + h_j s_{j-\frac{1}{2}}, \\
(R_5)_{j-\frac{1}{2}} &= v_{j-1} - v_j - \left(\frac{h_j}{\beta^*} \right) f_{j-\frac{1}{2}} v_{j-\frac{1}{2}} + \left(\frac{h_j}{\beta^*} \right) (u_{j-\frac{1}{2}})^2 - \left(\frac{h_j}{\beta^*} \right) [\lambda g_{j-\frac{1}{2}} + \delta q_{j-\frac{1}{2}}] \cos \alpha \\
&\quad - \left(\frac{\gamma}{\beta^*} \right) h_j u_{j-\frac{1}{2}}, \\
(R_6)_{j-\frac{1}{2}} &= p_{j-1} - p_j - h_j \text{Pr} (f_{j-\frac{1}{2}} p_{j-\frac{1}{2}}) - Nb h_j \text{Pr} (s_{j-\frac{1}{2}} p_{j-\frac{1}{2}}) - Nt h_j \text{Pr} (p_{j-\frac{1}{2}})^2, \\
(R_7)_{j-\frac{1}{2}} &= s_{j-1} - s_j - Le h_j (f_{j-\frac{1}{2}} s_{j-\frac{1}{2}}) + Nt_b (p_{j-1} - p_j),
\end{aligned} \tag{29}$$

where

$$\beta^* = \left(1 + \frac{1}{\beta} \right), \quad \gamma = M + K.$$

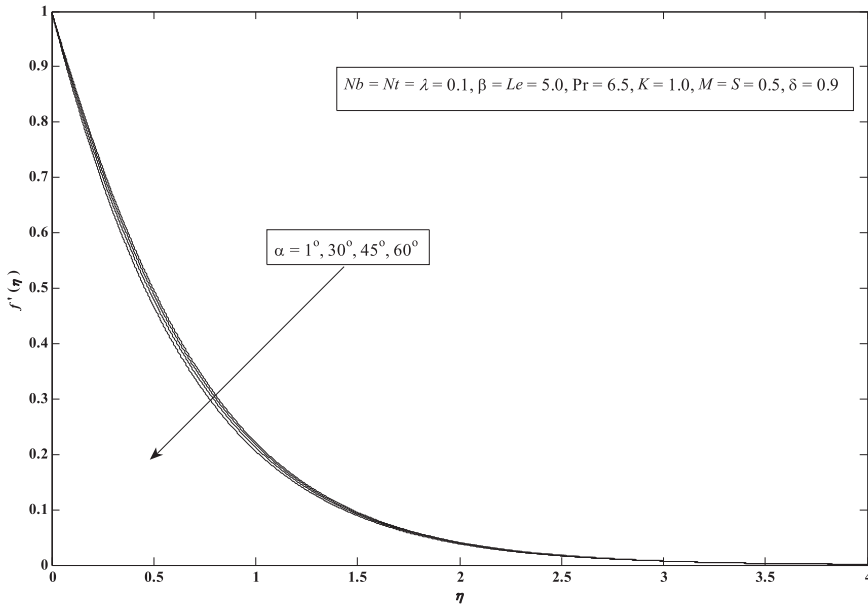


FIGURE 3 Variations of $f'(\eta)$ for distinct values of α

The boundary conditions are

$$\delta'f_0 = 0, \quad \delta'u_0 = 0, \quad \delta'g_0 = 0, \quad \delta'q_0 = 0, \quad \delta'u_j = 0, \quad \delta'g_j = 0, \quad \delta'q_j = 0. \quad (30)$$

3.3 | Block-elimination method

In vector-matrix form, differential equations of the system (28) can be defined by (Na, 1979)⁴³

$$[A][\delta'] = [r], \quad (31)$$

where

$$[A] = \begin{bmatrix} [A_1] & [C_1] & & & & & & \\ [B_2] & [A_2] & [C_2] & & & & & \\ & & & [B_{j-1}] & [A_{j-1}] & [C_{j-1}] & & \\ & & & & [B_j] & [C_j] & & \end{bmatrix} [\delta'] = \begin{bmatrix} [\delta'_1] \\ [\delta'_2] \\ \vdots \\ [\delta'_{j-1}] \\ [\delta'_j] \end{bmatrix}, \quad [r] = \begin{bmatrix} [r_1] \\ [r_2] \\ \vdots \\ r_{j-1} \\ r_j \end{bmatrix}. \quad (32)$$

Generally, the block-tridiagonal structure comprises constants or variables, but here, a remarkable thing can be seen, that is, for the Keller–Box process, it contains block matrices. By considering $e_j = -\frac{h_j}{2}$, the matrices take the following form:

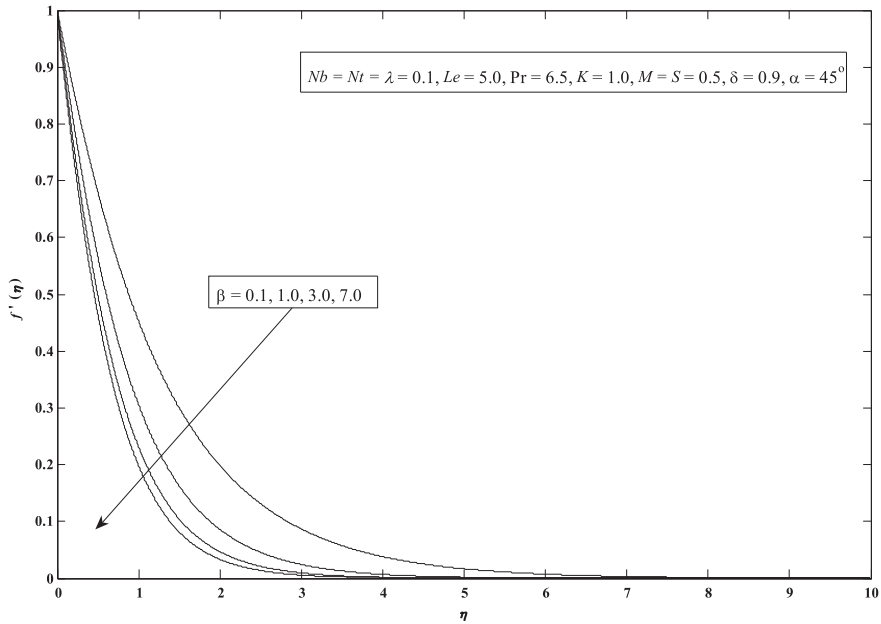


FIGURE 4 Variations of $f'(\eta)$ for distinct values of β

$$[A_1] = \begin{bmatrix} 0 & 0 & 0 & 1 & 0 & 0 & 0 \\ \frac{-h_1}{2} & 0 & 0 & 0 & \frac{-h_1}{2} & 0 & 0 \\ 0 & \frac{-h_1}{2} & 0 & 0 & 0 & \frac{-h_1}{2} & 0 \\ 0 & 0 & \frac{-h_1}{2} & 0 & 0 & 0 & \frac{-h_1}{2} \\ (a_2)_1 & 0 & 0 & (a_3)_1 & (a_1)_1 & 0 & 0 \\ 0 & (b_2)_1 & (b_6)_1 & (b_3)_1 & 0 & (b_1)_1 & (b_5)_1 \\ 0 & (c_6)_1 & (c_2)_1 & (c_3)_1 & 0 & (c_5)_1 & (c_1)_1 \end{bmatrix} \quad (33)$$

where $e_1 = \frac{-h_1}{2}$,

$$[A_1] = \begin{bmatrix} 0 & 0 & 0 & 1 & 0 & 0 & 0 \\ e_1 & 0 & 0 & 0 & e_1 & 0 & 0 \\ 0 & e_1 & 0 & 0 & 0 & e_1 & 0 \\ 0 & 0 & e_1 & 0 & 0 & 0 & e_1 \\ (a_2)_1 & 0 & 0 & (a_3)_1 & (a_1)_1 & 0 & 0 \\ 0 & (b_2)_1 & (b_6)_1 & (b_3)_1 & 0 & (b_1)_1 & (b_5)_1 \\ 0 & (c_6)_1 & (c_2)_1 & (c_3)_1 & 0 & (c_5)_1 & (c_1)_1 \end{bmatrix} \quad (34)$$

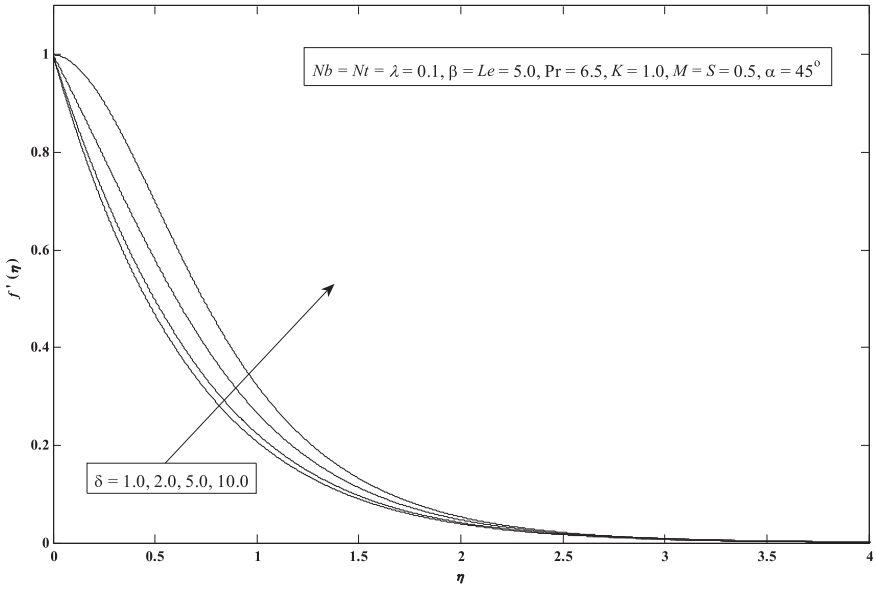


FIGURE 5 Variations of $f'(\eta)$ for distinct values of δ

$$[A_2] = \begin{bmatrix} \frac{-h_2}{2} & 0 & 0 & 1 & 0 & 0 & 0 \\ -1 & 0 & 0 & 0 & \frac{-h_2}{2} & 0 & 0 \\ 0 & -1 & 0 & 0 & 0 & \frac{-h_2}{2} & 0 \\ 0 & 0 & -1 & 0 & 0 & 0 & \frac{-h_2}{2} \\ (a_6)_2 & (a_8)_2 & (a_{10})_2 & (a_3)_2 & (a_1)_2 & 0 & 0 \\ 0 & 0 & 0 & (b_3)_2 & 0 & (b_1)_2 & (b_5)_2 \\ 0 & 0 & 0 & (c_3)_2 & 0 & (c_5)_2 & (c_1)_2 \end{bmatrix} \tag{35}$$

$$[A_j] = \begin{bmatrix} e_j & 0 & 0 & 1 & 0 & 0 & 0 \\ -1 & 0 & 0 & 0 & e_j & 0 & 0 \\ 0 & -1 & 0 & 0 & 0 & e_j & 0 \\ 0 & 0 & -1 & 0 & 0 & 0 & e_j \\ (a_6)_j & (a_8)_j & (a_{10})_j & (a_3)_j & (a_1)_j & 0 & 0 \\ 0 & 0 & 0 & (b_3)_j & 0 & (b_1)_j & (b_5)_j \\ 0 & 0 & 0 & (c_3)_j & 0 & (c_5)_j & (c_1)_j \end{bmatrix} \tag{36}$$

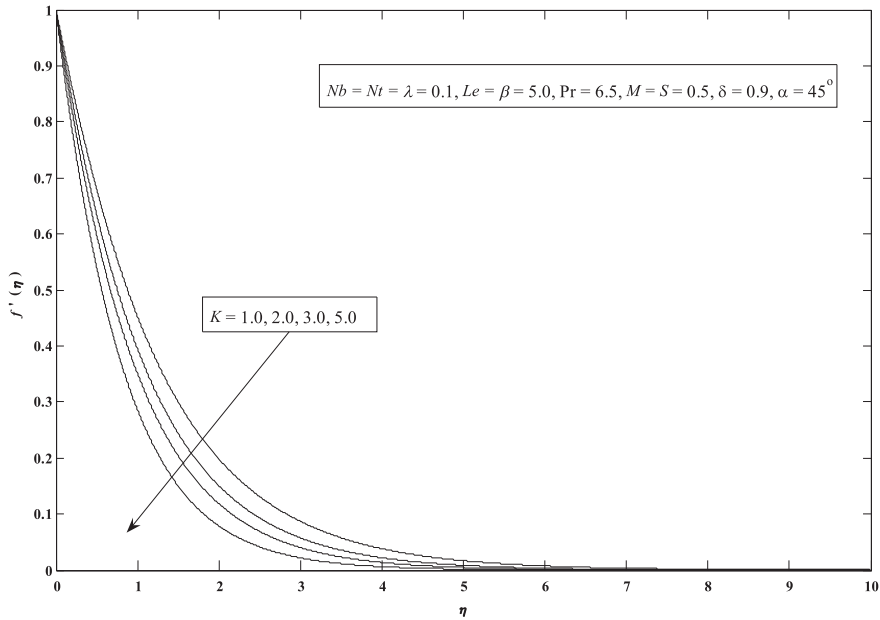


FIGURE 6 Variations of $f'(\eta)$ for distinct values of K

$$[B_j] = \begin{bmatrix} 0 & 0 & 0 & -1 & 0 & 0 & 0 \\ 0 & 0 & 0 & 0 & e_j & 0 & 0 \\ 0 & 0 & 0 & 0 & 0 & e_j & 0 \\ 0 & 0 & 0 & 0 & 0 & 0 & e_j \\ 0 & 0 & 0 & (a_4)_j & (a_2)_j & 0 & 0 \\ 0 & 0 & 0 & (b_4)_j & 0 & (b_2)_j & (b_6)_j \\ 0 & 0 & 0 & (c_4)_j & 0 & (c_6)_j & (c_2)_j \end{bmatrix} \quad 2 \leq j \leq J \quad (37)$$

$$[C_j] = \begin{bmatrix} e_j & 0 & 0 & 0 & 0 & 0 & 0 \\ 1 & 0 & 0 & 0 & 0 & 0 & 0 \\ 0 & 1 & 0 & 0 & 0 & 0 & 0 \\ 0 & 0 & 1 & 0 & 0 & 0 & 0 \\ (a_5)_j & (a_7)_j & (a_9)_j & 0 & 0 & 0 & 0 \\ 0 & 0 & 0 & 0 & 0 & 0 & 0 \\ 0 & 0 & 0 & 0 & 0 & 0 & 0 \end{bmatrix} \quad 1 \leq j \leq J - 1 \quad (38)$$

4 | RESULTS AND DISCUSSIONS

This section contains the discussions and elucidations of our results in graphical and numeric forms. The Keller–Box method is applied to solve the ordinary differential system (Equations (8)–(10)) with condition (12). The numerical result of the concerned physical factors such as Brownian movement Nb , Casson constraint β , thermophoretic Nt , Lewis number Le , magnetic parameter M , permeability parameter K , buoyancy parameter λ , Prandtl number Pr , solutal buoyancy parameter δ , inclination parameter α , and suction constraint S are elaborated in tabular and graphical form. In Table 1, with the lack of buoyancy constraints λ , the solutal

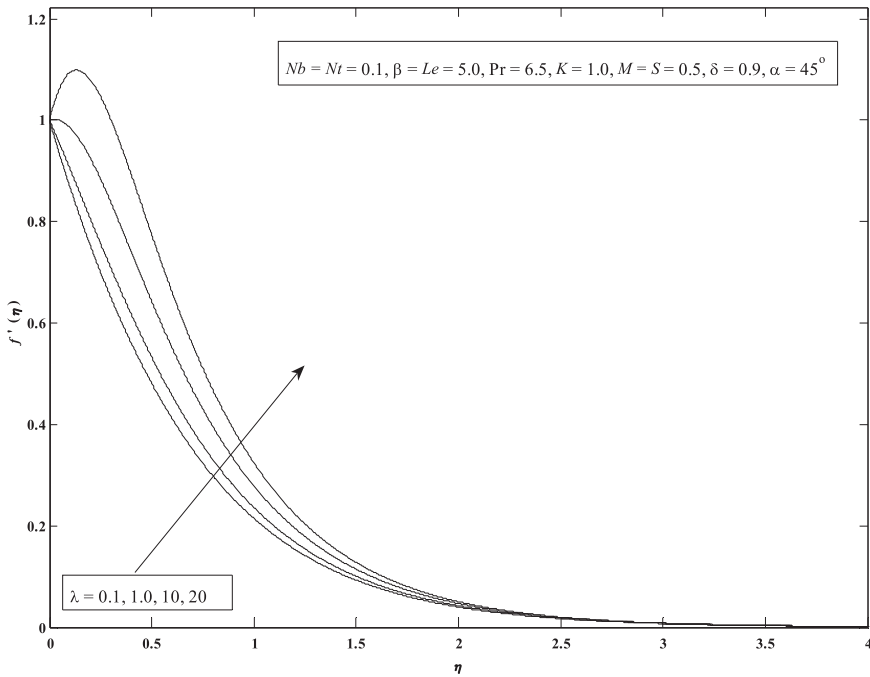


FIGURE 7 Variations of $f'(\eta)$ for distinct values of λ

buoyancy parameter δ with $\alpha = 90^\circ$ when $\beta \rightarrow \infty$ results in $-\theta'(0)$ and $-\varphi'(0)$ is matched with the existing results.⁴¹ The outcomes showed excellent agreement. The effects of $-\theta'(0)$, $-\varphi'(0)$, and $C_{fx}(0)$ for distinct values of the arising constraints Nb , Nt , β , M , K , λ , δ , α , Pr , Le , and S are mentioned in Table 2. It is evaluated that $-\theta'(0)$ is retarded by decrement in Nb , Nt , K , S , and

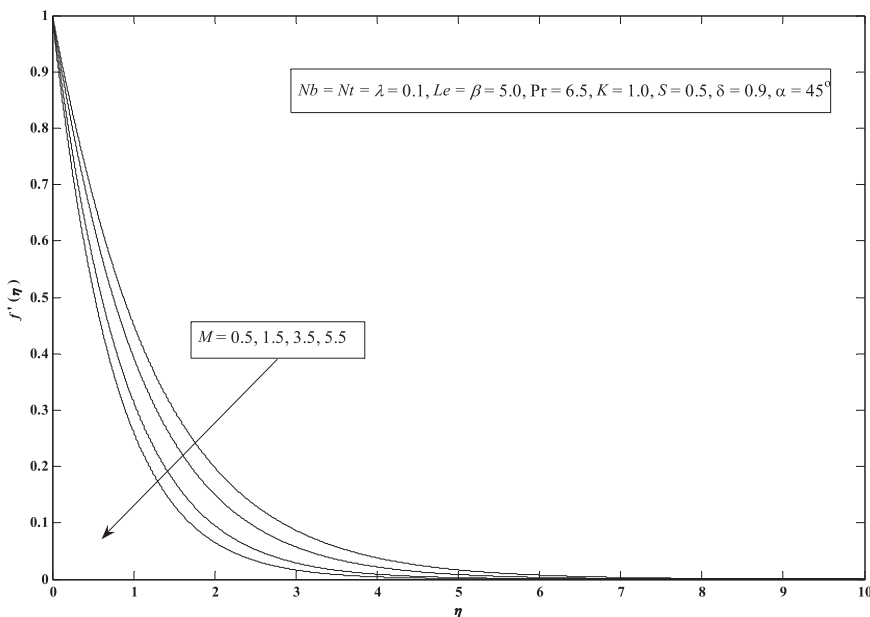


FIGURE 8 Variations of $f'(\eta)$ for distinct values of M

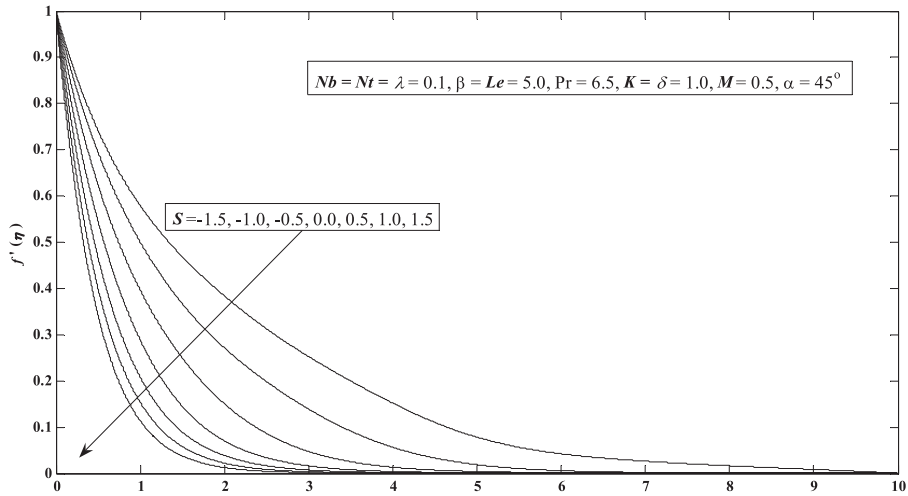


FIGURE 9 Variations of $f'(\eta)$ for distinct values of S

increasing the values of Le , M , β , and α . On the other hand, $-\theta'(0)$ rises by increasing the values of Pr , λ , and S . Besides this, we noticed that $-\phi'(0)$ increases with falling Nb , δ , and increasing Le , λ , S . Whereas, $-\phi'(0)$ drops by lowering the values of K , S , and increasing Pr , M , β , and γ . We further visualized that $C_{fx}(0)$ rises for the lesser Nb , K , and for big Pr , Le , M , β , δ , and α . Moreover, it is found that $C_{fx}(0)$ decreases by lessening the values of δ , S and by increasing λ .

Figure 3 shows that the velocity distribution $f'(\eta)$ decreases with increasing the inclination parameter. This can be ascribed to the circumstances that inclination angle drops as the result of buoyant force because of thermal diffusion with the influence of $\cos \alpha$. Accordingly, the liquid driving force declines due to which velocity of the fluid drops. The nature of Casson

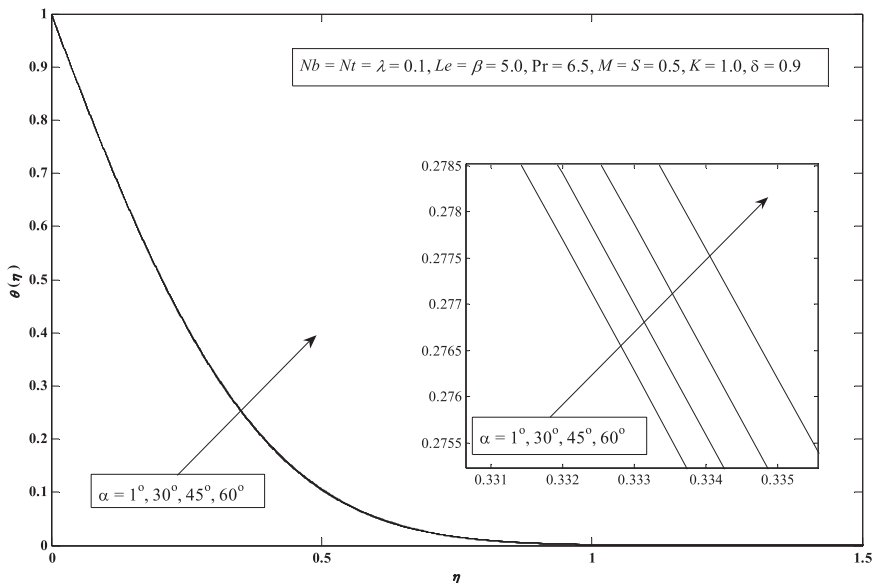


FIGURE 10 Variations of $\theta(\eta)$ for distinct values of α

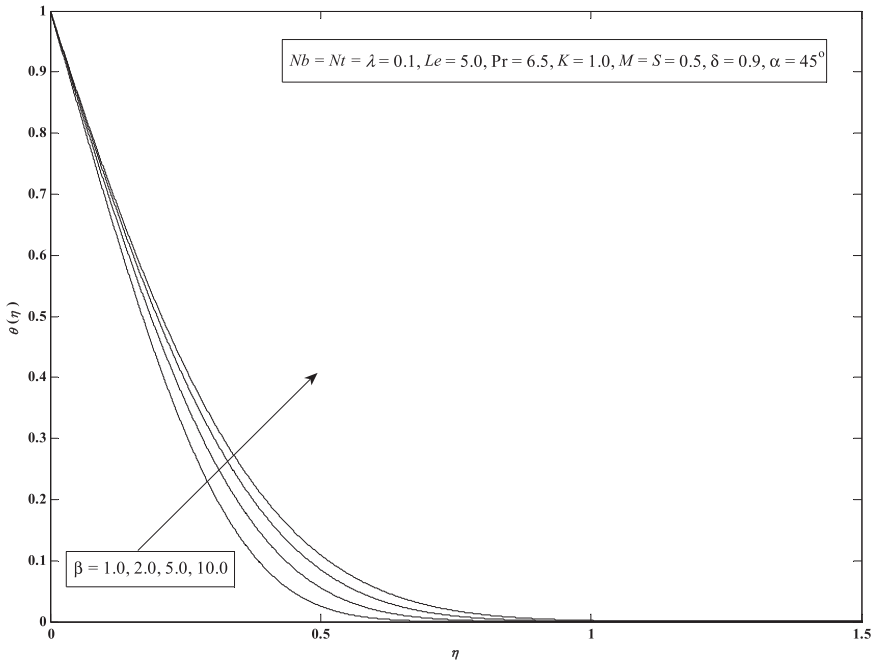


FIGURE 11 Variations of $\theta(\eta)$ for distinct values of β

constraint on velocity distribution, $f'(\eta)$, is presented in Figure 4. Velocity distribution is retarded for emerging values of the Casson constraint. Physically, the enlarging Casson constraint β corresponds to stronger viscosity, that is, reduction in yield stress. Therefore, the momentum layer of thickness is reduced. Figure 5 indicates that the velocity outline increases

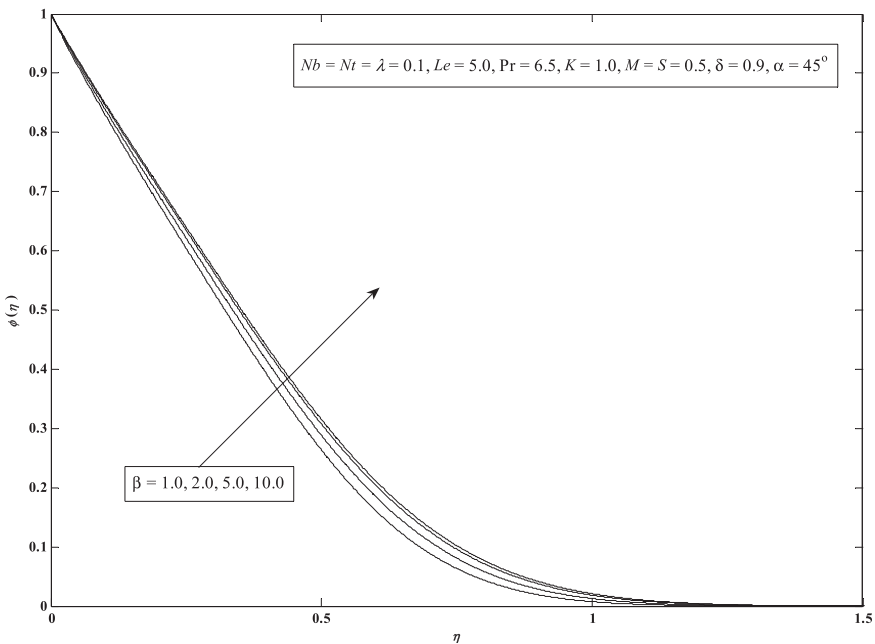


FIGURE 12 Variations of $\phi(\eta)$ for distinct values of β

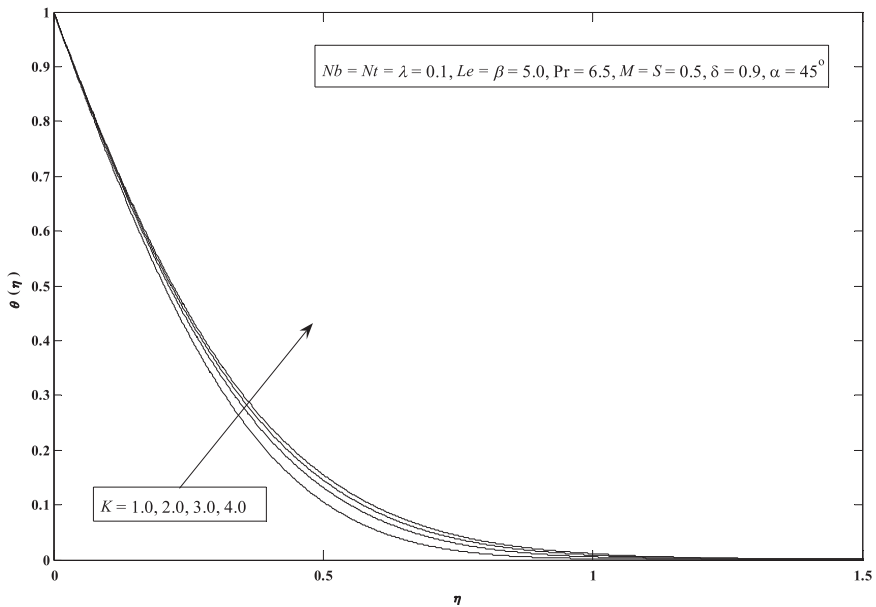


FIGURE 13 Variations of $\theta(\eta)$ for distinct values of K

by enhancing the solutal buoyancy factor. Physically, the length, concentration difference, and kinematic viscosity of the liquid affect the factor δ . On the other hand, there is an opposite relation between the viscosity and velocity of the fluid. Therefore, the viscosity of the fluid drops on rising the magnitude of δ , and the concentration increases directly due to which the velocity field upsurges. Finally, the factor δ shows a direct relation with the velocity outline. Figure 6 describes the velocity profile falls with increasing the permeability parameter K . The impacts of

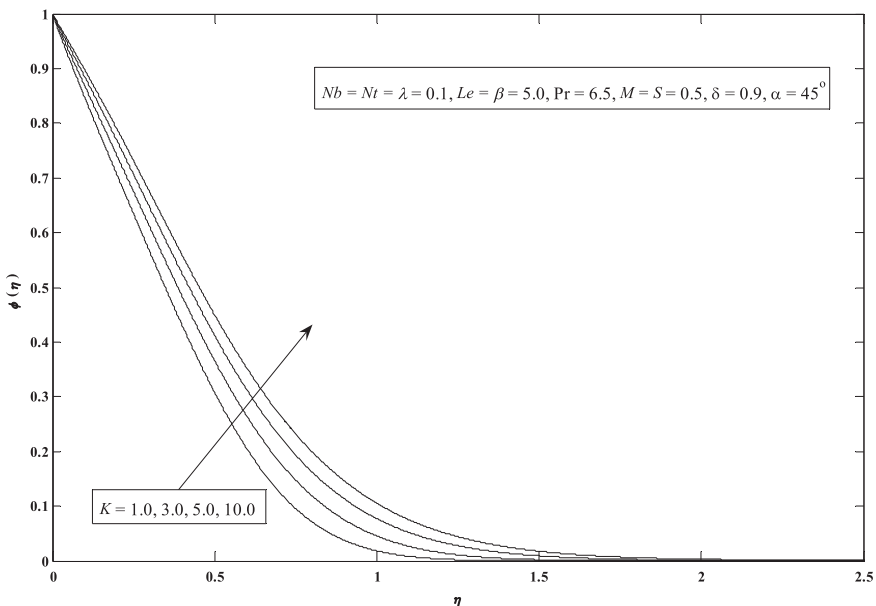


FIGURE 14 Variations of $\phi(\eta)$ for distinct values of K

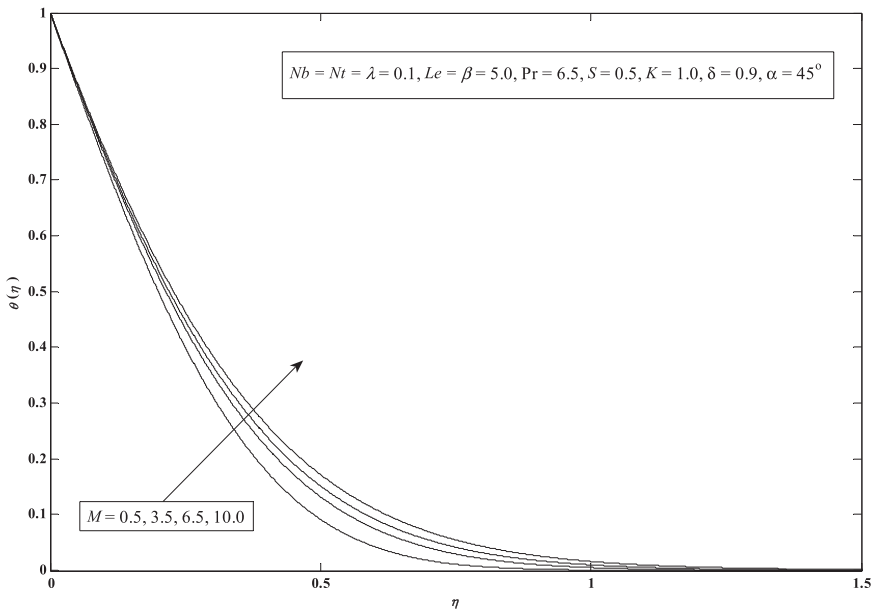


FIGURE 15 Variations of $\theta(\eta)$ for distinct values of M

buoyancy factor are shown in Figure 7. Velocity distribution $f'(\eta)$ rises by improving the buoyancy limit. Physically, the growing magnitude of the buoyancy forces decreases the viscous force, which favors the fluid flow, which causes faster motion. The impressions of M are described in Figure 8. The velocity shape falls with increasing the magnetic element M .

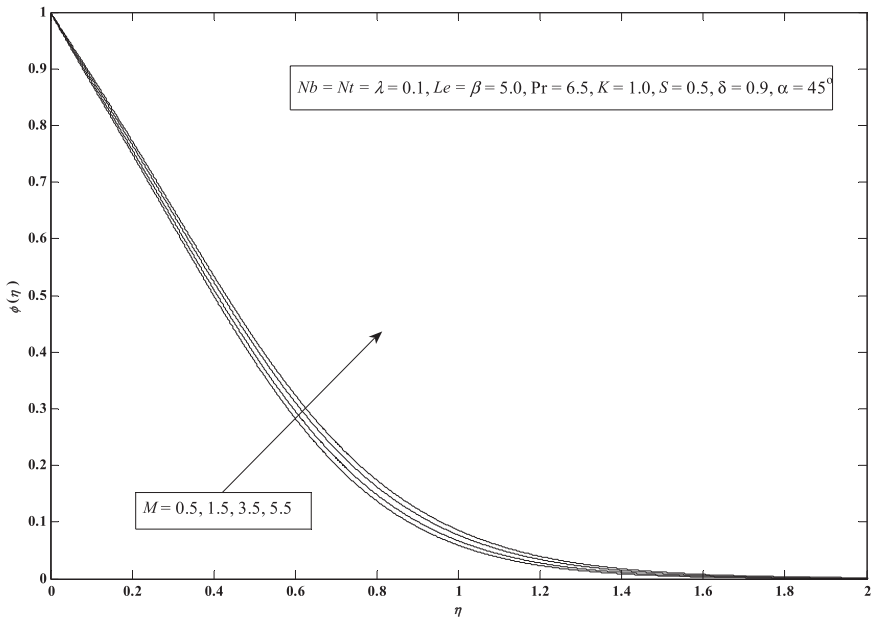


FIGURE 16 Variations of $\phi(\eta)$ for distinct values of M

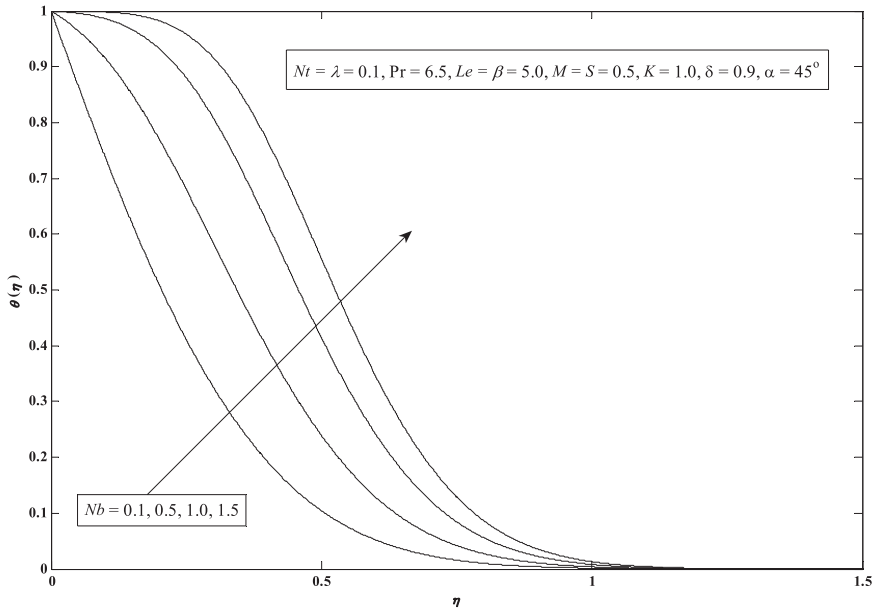


FIGURE 17 Variations of $\theta(\eta)$ for distinct values of Nb

Physically, an enhancement in M refers to improving the Lorentz force, which decreases the velocity. The characterization S on the velocity $f'(\eta)$ is shown in Figure 9. It is evident that $f'(\eta)$ decreases with increasing the suction constraint. Moreover, Figure 10 indicates the variations of temperature profile for the inclination parameter. Temperature increases by

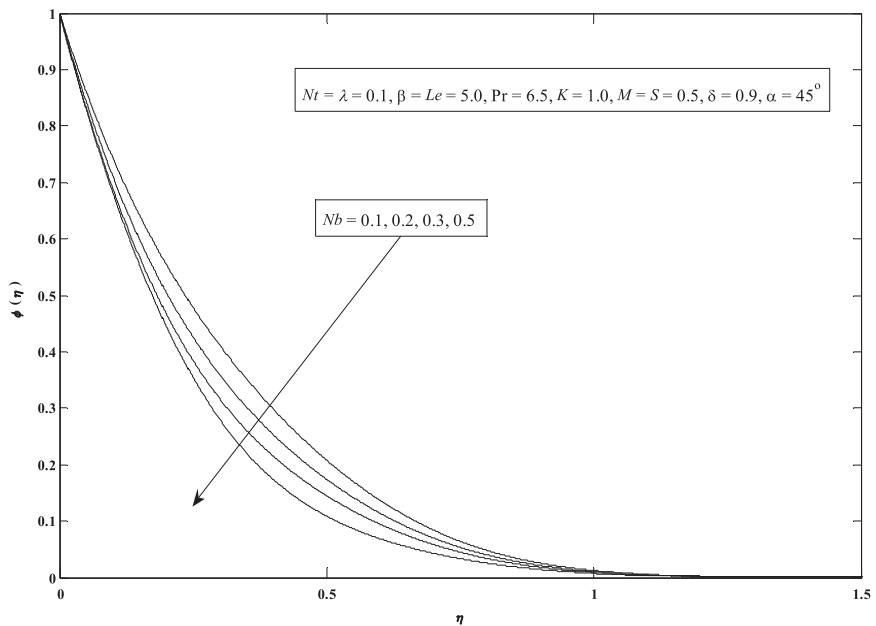


FIGURE 18 Variations of $\phi(\eta)$ for distinct values of Nb

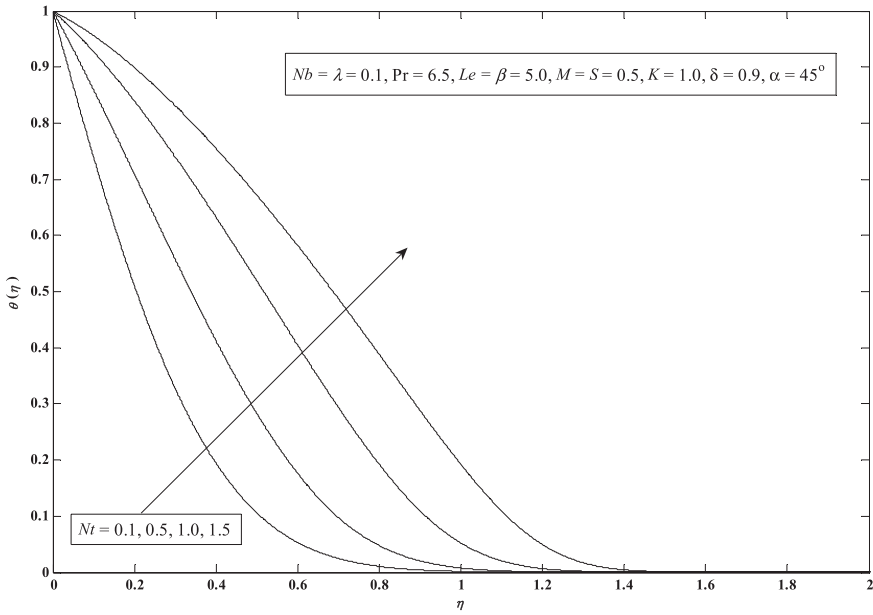


FIGURE 19 Variations of $\theta(\eta)$ for distinct values of Nt

enhancing the values of the inclination constraint. Variations of Casson constraint β on temperature $\theta(\eta)$ and concentration $\phi(\eta)$ profiles are shown in Figures 11 and 12. A larger Casson constraint β boosts up the temperature $\theta(\eta)$ and concentration $\phi(\eta)$ distributions. Similar patterns are shown in Figures 13 and 14 for distinct K . Furthermore, Figures 15 and 16

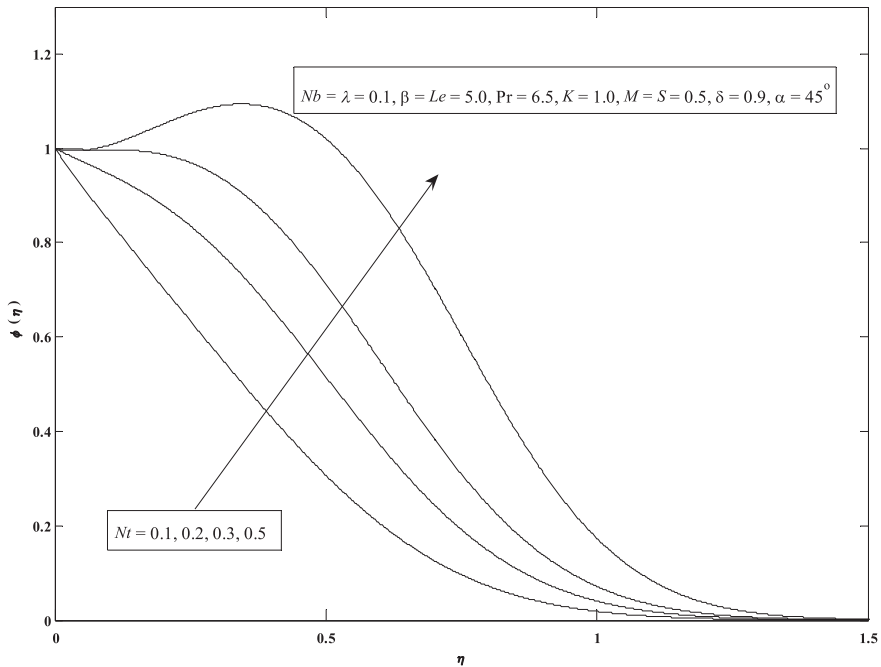


FIGURE 20 Variations of $\phi(\eta)$ for distinct values of Nt

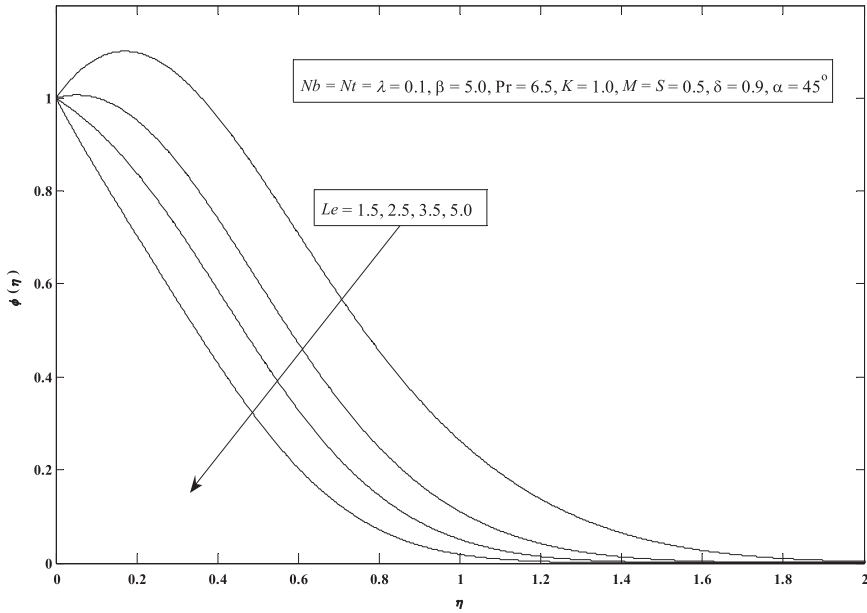


FIGURE 21 Variations of $\phi(\eta)$ for distinct values of Le

depict temperature $\theta(\eta)$ and concentration $\phi(\eta)$ profiles increase for a larger magnetic parameter M .

Figures 17 and 18 indicate the effect of Brownian movement on $\theta(\eta)$ and $\phi(\eta)$. We visualized that the temperature distribution enlarges with an enhancement in Brownian motion. On the

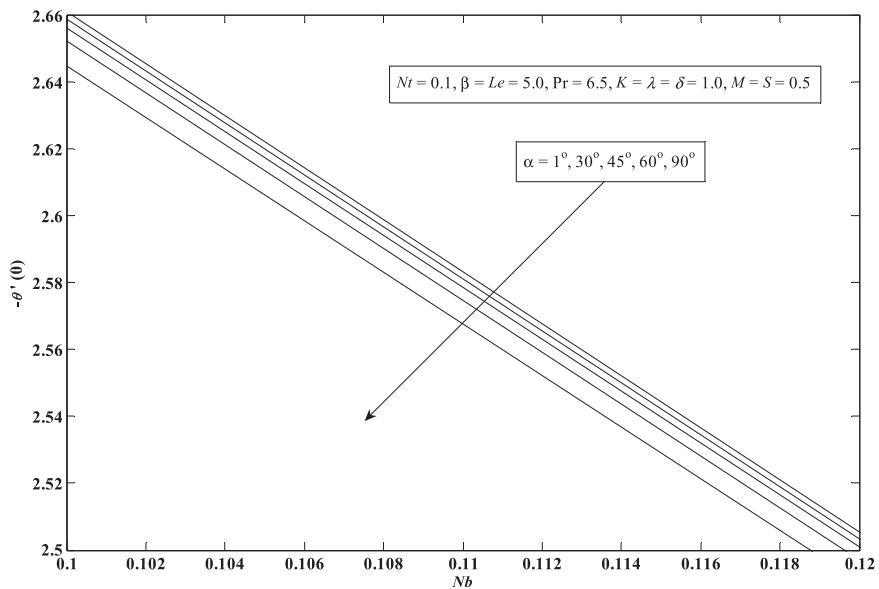


FIGURE 22 Variations of $-\theta'(0)$ for distinct values of Nb and α

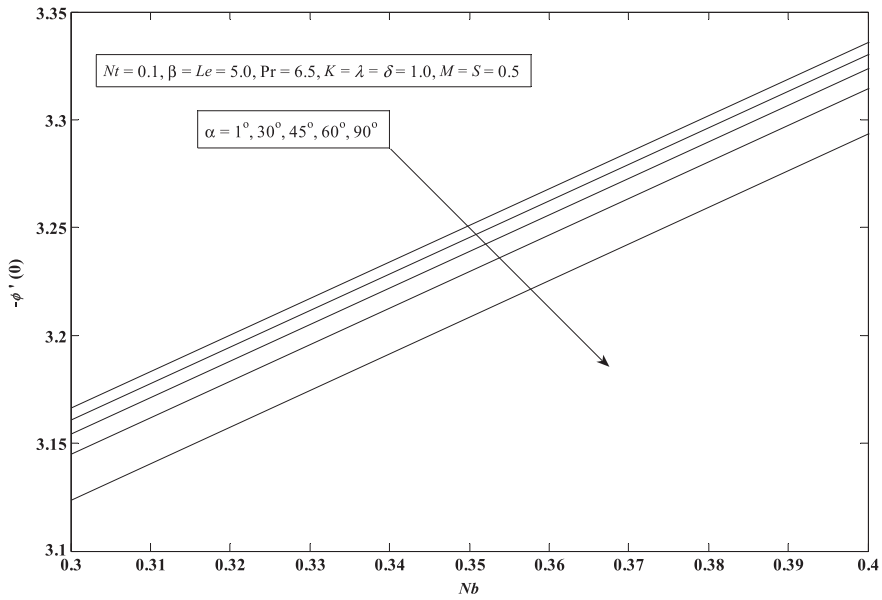


FIGURE 23 Variations of $-\phi'(0)$ for distinct values of Nb and α

other hand, the opposite effect is seen on the distribution of $\phi(\eta)$. Physically, the enlargement in Brownian constraint supports heating up the boundary-layer, which makes nanoparticles travel from the stretching sheet to the motionless liquid. Therefore, the concentration of the nanoparticles is moderated. Figures 19 and 20 represent the nature of Nt on $\theta(\eta)$, δ , and $\phi(\eta)$.

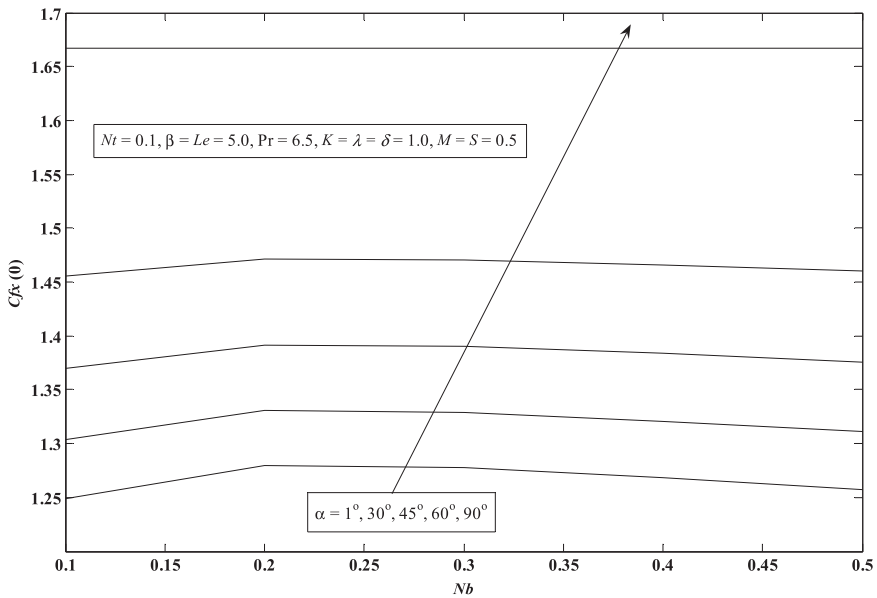


FIGURE 24 Variations of $C_{fx}(0)$ for distinct values of Nb and α

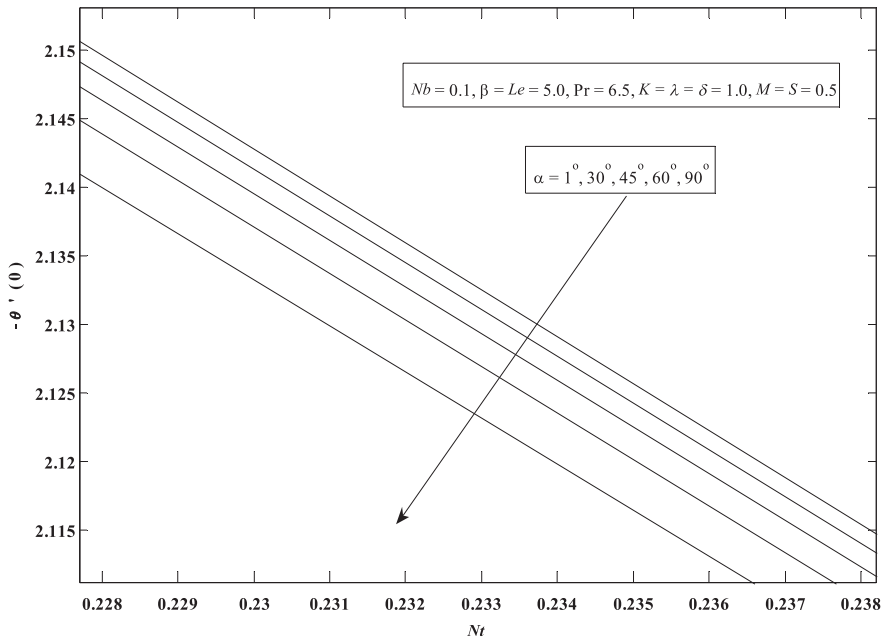


FIGURE 25 Variations of $-\theta'(0)$ for distinct values of Nt and α

These figures show that both $\theta(\eta)$ and $\phi(\eta)$ increase for the incrementing values of the thermophoresis constraint. Figure 21 elucidates the changes in $\phi(\eta)$ profile for distinct Le . The thickness layer retards by enhancing the values of Le . Figures 22 to 27 show that $-\theta'(0)$ and $-\phi'(0)$ decrease by increasing the inclination values while $C_{fx}(0)$ increases by increasing the inclination.

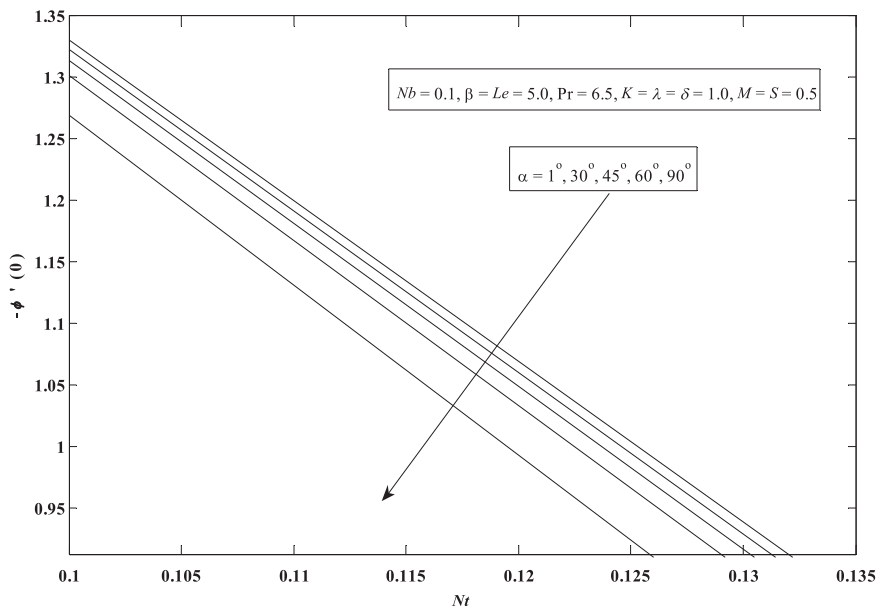


FIGURE 26 Variations of $-\phi'(0)$ for distinct values of Nt and α

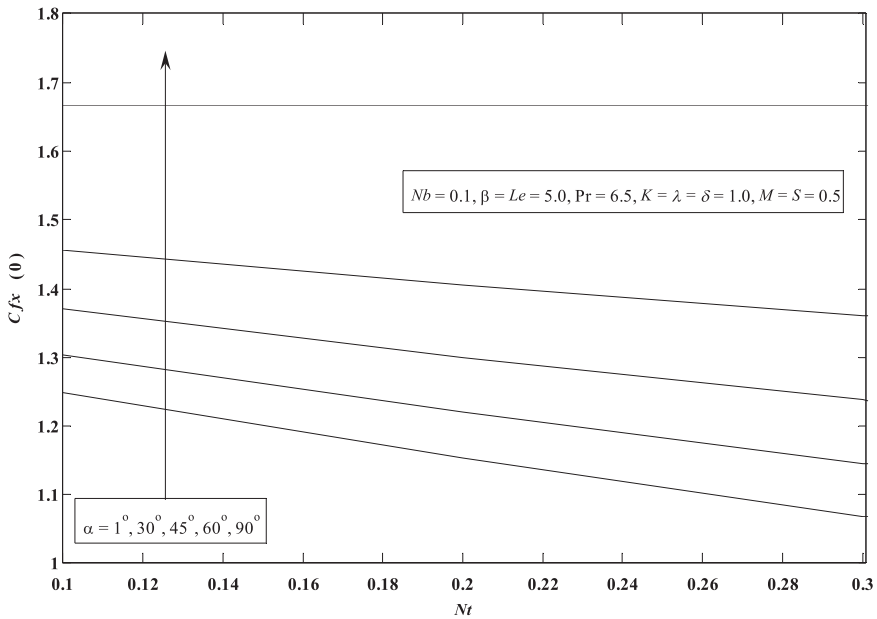


FIGURE 27 Variations of $C_{fx}(0)$ for distinct values of Nt and α

5 | CONCLUSIONS

Heat mass transport analysis of Casson nanomaterial flow induced by the inclination of surface under the existence of magnetic field is communicated in this study. We revealed that $-\theta'(0)$ decreases for the growing values of Nb , Nt , K , and rises for larger values of Le , M , β , α , Pr , λ , and S . Furthermore, it is evaluated that the reduced Sherwood number $-\phi'(0)$ increases for increasing values of Nb , δ , Le , λ , S . The values of $C_{fx}(0)$ increase for the weaker Nb , K and higher values of Pr , Le , M , β , δ , and α correspond to decrement in this. On the other hand, by increasing the values of Pr , the temperature profile drops because the thermal thickness of layer decreases with enhancing the Pr .

NOMENCLATURE

g	acceleration due to gravity
B_0	uniform magnetic field strength
σ	electrical conductivity
μ	viscosity
ρ_f	base-fluid density
ρ_p	nanoparticle density
β	Casson constraint
β_t	thermal expansion coefficient
β_c	concentration expansion coefficient
D_B	Brownian diffusion coefficient
D_T	thermophoresis diffusion coefficient
k	thermal conductivity
$(\rho c)_p$	heat capacitance of the nanoparticles

$(\rho c)_f$	heat capacitance of the base fluid
$\alpha^* = k/(\rho c)_f$	thermal diffusivity parameter
S	suction parameter
M	Hartmann number
ν	kinematic viscosity
Pr	Prandtl number
Le	Lewis number
K	permeability parameter
$-\theta'(0)$	reduced Nusselt number
$-\phi'(0)$	reduced Sherwood number
$C_{fx}(0)$	skin friction coefficient
$Re_x = (u_w(x)x)/\nu$	local Reynolds number
Nb	Brownian motion parameter
Nt	thermophoresis parameter
λ	buoyancy parameter
δ	solulal buoyancy parameter
α	inclination parameter
$\tau = (\rho c)_p/(\rho c)_f$	ratio of effective heat capacity of nanoparticle and heat capacity of liquid

ORCID

Sabir Ali Shehzad  <http://orcid.org/0000-0001-8359-9706>

REFERENCES

1. Sakiadis BC. Boundary-layer behavior on continuous solid surfaces: I. Boundary-layer equations for two-dimensional and axisymmetric flow. *AIChE J.* 1961;7:26-28.
2. Crane LJ. Flow past a stretching plate. *Zeitschrift Für Angewandte Mathematik Und Physik.* 1970;21:645-647.
3. Mucoglu A, Chen TS. Mixed convection on inclined surfaces. *J Heat Transfer Transac ASME.* 1979;101:422-426.
4. Chamkha AJ, Khaled ARA. Similarity solutions for hydromagnetic simultaneous heat and mass transfer by natural convection from an inclined plate with internal heat generation or absorption. *Heat Mass Transfer.* 2001;37:117-123.
5. Alam MS, Rahman MM, Sattar MA. MHD free convective heat and mass transfer flow past an inclined surface with heat generation. *Thammasat Int J Sci Technol.* 2006;11:1-8.
6. Ramesh GK, Giresha BJ, Bagewadi CS. Heat transfer in MHD dusty boundary layer flow over an inclined stretching sheet with non-uniform heat source/sink. *Adv Math Phys.* 2012;2012:657805.
7. Ali F, Khan I, Samiulhaq, Shafie S. Conjugate effects of heat and mass transfer on MHD free convection flow over an inclined plate embedded in a porous medium. *PLoS One.* 2013;8:e65223.
8. Ali M, Alim MDA, Alam MS. Heat transfer boundary layer flow past an inclined stretching sheet in the presence of magnetic field. *Int J Adv Res Technol.* 2014;3:34-40.
9. Suriyakumar P, Devi SPA. Effects of suction and internal heat generation on hydromagnetic mixed convective nanofluid flow over an inclined stretching plate. *Eur J Adv Eng Technol.* 2015;2:51-58.
10. Malik MY, Rehman K. Effects of second order chemical reaction on MHD free convection dissipative fluid flow past an inclined porous surface by way of heat generation: A Lie group analysis. *Inform Sci Lett.* 2016;45:35-45.
11. Hayat T, Qayyum S, Alsaedi A, Asghar S. Radiation effects on the mixed convection flow induced by an inclined stretching cylinder with non-uniform heat source/sink. *PLoS One.* 2017;12:e0175584.

12. Parmar A. Unsteady convective boundary layer flow for MHD Williamson fluid over an inclined porous stretching sheet with non-linear radiation and heat source. *Int J Appl Computa Math.* 2017;3:859-881.
13. Choi SUS, Eastman JA. Enhancing thermal conductivity of fluids with nanoparticles. *ASME Int Mech Eng Congr Expo.* 1995;66:99-105.
14. Buongiorno J. Convective transport in nanofluids. *J Heat Transfer.* 2006;128:240-250.
15. Murthy PVS, Sutradhar A, RamReddy C. Double-diffusive free convection flow past an inclined plate embedded in a non-Darcy porous medium saturated with a nanofluid. *Transp Porous Media.* 2013;98(3):553-564.
16. Rashad AM. Unsteady nanofluid flow over an inclined stretching surface with convective boundary condition and anisotropic slip impact. *Int J Heat Technol.* 2017;35(1):82-90.
17. Usman M, Soomro FA, Haq RU, Wang W, Deferli O. Thermal and velocity slip effects on Casson nanofluid flow over an inclined permeable stretching cylinder via collocation method. *Int J Heat Mass Transfer.* 2018;122:1255-1263.
18. Khan M, Shahid A, Malik MY, Salahuddin T. Thermal and concentration diffusion in Jeffery nanofluid flow over an inclined stretching sheet: A generalized Fourier's and Fick's perspective. *J Mol Liq.* 2018;251:7-14.
19. Ghadikolaei SS, Hosseinzadeh K, Ganji DD, Jafari B. Nonlinear thermal radiation effect on magneto Casson nanofluid flow with Joule heating effect over an inclined porous stretching sheet. *Case Stud Therm Eng.* 2018;12:176-187.
20. Ziaei-Rad M, Kasaeipoor A, Rashidi MM, Lorenzini G. A similarity solution for mixed-convection boundary layer nanofluid flow on an inclined permeable surface. *J Therm Sci Eng Appl.* 2017;9:021015.
21. Waqas H, Khan SU, Shehzad SA, Imran M. Radiative flow of Maxwell nanofluids containing gyrotactic microorganism and energy activation with convective Nield conditions. *Heat Transfer-Asian Res.* 2019;48:1663-1687.
22. Manjunatha S, Kumar KG, Gireesha BJ, Abbasi FM, Shehzad SA. Numerical illustrations on 3D flow of tangent hyperbolic liquid past a bidirectional moving sheet with convective heat transfer at the boundary. *Heat Transfer-Asian Res.* 2019;48:1899-1912.
23. Ameen Ibni, Shah Z, Islam S, et al. Hall and ion-slip effect on CNTS nanofluid over a porous extending surface through heat generation and absorption. *Entropy.* 2019;21(8):801.
24. Dawar A, Shah Z, Kumam P, Khan W, Islam S. Influence of MHD on thermal behavior of Darcy-Forchheimer nanofluid thin film flow over a nonlinear stretching disc. *Coatings.* 2019;9(7):446.
25. Jawad M, Shah Z, Khan A, Khan W, Kumam P, Islam S. Entropy generation and heat transfer analysis in MHD unsteady rotating flow for aqueous suspensions of carbon nanotubes with nonlinear thermal radiation and viscous dissipation effect. *Entropy.* 2019;21(5):492.
26. Shah Z, Shafee A, Al-Qawasmi AR, Thili I. Time dependent heat transfer in a finned triplex tube during phase changing of nanoparticle enhanced PCM. *Eur Phys J Plus.* 2019;134:173.
27. Sha Zahir, Dawar A, Alzahrani E, Kumam P, Khan AJ, Islam S. Hall effect on couple stress 3D nanofluid flow over an exponentially stretched surface with Cattaneo Christov heat flux model. *IEEE Access.* 2019;7:64844-64855.
28. Jawad M, Shah Z, Khan A, Islam S, Ullah H. Three-dimensional magnetohydrodynamic nanofluid thin-film flow with heat and mass transfer over an inclined porous rotating disk. *Adv Mech Eng.* 2019;11(8), <https://doi.org/10.1177/1687814019869757>
29. Nasir S, Shah Z, Islam S, et al Three dimensional Darcy-Forchheimer radiated flow of single and multiwall carbon nanotubes over a rotating stretchable disk with convective heat generation and absorption. *AIP Adv.* 2019;9(3):035031.
30. Gul T, Nasir S, Islam S, Shah Z, Khan MA. Effective prandtl number model influences on the Al₂O₃-H₂O and Al₂O₃-C₂H₆O₂ nanofluids spray along a stretching cylinder. *Arab J Sci Eng.* 2019;44(2):1601-1616.
31. Kumar MS, Sandeep N, Kumar BR, Saleem S. A comparative study of chemically reacting 2D flow of Casson and Maxwell fluids. *Alexandria Eng J.* 2018;57:2027-2034.
32. Alkawasbeh HT. Numerical solution of micropolar Casson fluid behaviour on steady MHD natural convective flow about a solid sphere. *J Adv Res Fluid Mech Therm Sci.* 2018;50:55-66.
33. Reddy PBA. Magnetohydrodynamic flow of a Casson fluid over an exponentially inclined permeable stretching surface with thermal radiation and chemical reaction. *Ain Shams Eng J.* 2016;7(2):593-602.

34. Saeed Anwar, Shah Z, Islam S, et al. Three-dimensional Casson nanofluid thin film flow over an inclined rotating disk with the impact of heat generation/consumption and thermal radiation. *Coatings*. 2019;9(4):248.
35. Rawi NA, Ilias MR, Lim YJ, Isa ZM, Shafie S. Unsteady mixed convection flow of Casson fluid past an inclined stretching sheet in the presence of nanoparticles. *J Phys Conf Ser*. 2017;890(1). IOP Publishing.
36. Shehzad SA, Hayat T, Qasim M, Asghar S. Effects of mass transfer on MHD flow of Casson fluid with chemical reaction and suction. *Braz J Chem Eng*. 2013;30:187-195.
37. Gopal D, Kishan N, Raju CSK. Viscous and Joule's dissipation on Casson fluid over a chemically reacting stretching sheet with inclined magnetic field and multiple slips. *Inform Med Unlock*. 2017;9:154-160.
38. Shah Z, Islam S, Ayaz H, Khan S. Radiative heat and mass transfer analysis of micropolar nanofluid flow of Casson fluid between two rotating parallel plates with effects of Hall current. *J Heat Transfer*. 2019;141(2):022401.
39. Raju RS. Unsteady MHD boundary layer flow of Casson fluid over an inclined surface embedded in a porous medium with thermal radiation and chemical reaction. *J Nanofluids*. 2018;7(4):694-703.
40. Souayah B, Reddy MG, Sreenivasulu P, Poornima T, Rahimi-Gorji M, Alarifi IM. Comparative analysis on non-linear radiative heat transfer on MHD Casson nanofluid past a thin needle. *J Mol Liq*. 2019;284:163-174.
41. Khan W, Pop I. Boundary-layer flow of a nanofluid past a stretching sheet. *Int J Heat Mass Transfer*. 2010;53:24772483.
42. Keller HB, Cebeci T. Accurate numerical methods for boundary-layer flows. II: Two dimensional turbulent flows. *AIAA J*. 1972;10(9):1193-1199.
43. Na TY. *Computational Methods in Engineering Boundary Value Problem*. New York: Academic Press; 1979.

How to cite this article: Anwar MI, Rafique K, Misiran M, Shehzad SA. Numerical study of hydrodynamic flow of a Casson nanomaterial past an inclined sheet under porous medium. *Heat Transfer—Asian Res*. 2019;1–28. <https://doi.org/10.1002/htj.21614>